





Bacterial Swarming Reduces *Proteus mirabilis* and *Vibrio parahaemolyticus* Cell Stiffness and Increases β -Lactam Susceptibility

George K. Auer,^a Piercen M. Oliver,^b Manohary Rajendram,^b Ti-Yu Lin,^b Qing Yao,^{c,d}  Grant J. Jensen,^{c,d}  Douglas B. Weibel^{a,b,e}

^aDepartment of Biomedical Engineering, University of Wisconsin—Madison, Madison, Wisconsin, USA

^bDepartment of Biochemistry, University of Wisconsin—Madison, Madison, Wisconsin, USA

^cDivision of Biology and Biological Engineering, California Institute of Technology, Pasadena, California, USA

^dHoward Hughes Medical Institute, California Institute of Technology, Pasadena, California, USA

^eDepartment of Chemistry, University of Wisconsin—Madison, Madison, Wisconsin, USA

ABSTRACT Swarmer cells of the Gram-negative uropathogenic bacteria *Proteus mirabilis* and *Vibrio parahaemolyticus* become long (>10 to $100\ \mu\text{m}$) and multinucleate during their growth and motility on polymer surfaces. We demonstrated that the increasing cell length is accompanied by a large increase in flexibility. Using a microfluidic assay to measure single-cell mechanics, we identified large differences in the swarmer cell stiffness (bending rigidity) of *P. mirabilis* ($5.5 \times 10^{-22}\ \text{N m}^2$) and *V. parahaemolyticus* ($1.0 \times 10^{-22}\ \text{N m}^2$) compared to vegetative cells ($1.4 \times 10^{-20}\ \text{N m}^2$ and $2.2 \times 10^{-22}\ \text{N m}^2$, respectively). The reduction in bending rigidity (~ 2 -fold to ~ 26 -fold) was accompanied by a decrease in the average polysaccharide strand length of the peptidoglycan layer of the cell wall from 28 to 30 disaccharides to 19 to 22 disaccharides. Atomic force microscopy revealed a reduction in *P. mirabilis* peptidoglycan thickness from 1.5 nm (vegetative cells) to 1.0 nm (swarmer cells), and electron cryotomography indicated changes in swarmer cell wall morphology. *P. mirabilis* and *V. parahaemolyticus* swarmer cells became increasingly sensitive to osmotic pressure and susceptible to cell wall-modifying antibiotics (compared to vegetative cells)—they were $\sim 30\%$ more likely to die after 3 h of treatment with MICs of the β -lactams cephalexin and penicillin G. The adaptive cost of “swarming” was offset by the increase in cell susceptibility to physical and chemical changes in their environment, thereby suggesting the development of new chemotherapies for bacteria that leverage swarming for the colonization of hosts and for survival.

IMPORTANCE *Proteus mirabilis* and *Vibrio parahaemolyticus* are bacteria that infect humans. To adapt to environmental changes, these bacteria alter their cell morphology and move collectively to access new sources of nutrients in a process referred to as “swarming.” We found that changes in the composition and thickness of the peptidoglycan layer of the cell wall make swarmer cells of *P. mirabilis* and *V. parahaemolyticus* more flexible (i.e., reduce cell stiffness) and that they become more sensitive to osmotic pressure and cell wall-targeting antibiotics (e.g., β -lactams). These results highlight the importance of assessing the extracellular environment in determining antibiotic doses and the use of β -lactam antibiotics for treating infections caused by swarmer cells of *P. mirabilis* and *V. parahaemolyticus*.

KEYWORDS antibiotics, bacterial cell mechanics, bacterial swarming, osmotic pressure, peptidoglycan

Citation Auer GK, Oliver PM, Rajendram M, Lin T-Y, Yao Q, Jensen GJ, Weibel DB. 2019. Bacterial swarming reduces *Proteus mirabilis* and *Vibrio parahaemolyticus* cell stiffness and increases β -lactam susceptibility. mBio 10:e00210-19. <https://doi.org/10.1128/mBio.00210-19>.

Invited Editor Joshua Shaevitz, Princeton University

Editor Margaret J. McFall-Ngai, University of Hawaii at Manoa

Copyright © 2019 Auer et al. This is an open-access article distributed under the terms of the [Creative Commons Attribution 4.0 International license](https://creativecommons.org/licenses/by/4.0/).

Address correspondence to Douglas B. Weibel, douglas.weibel@wisc.edu.

Received 4 February 2019

Accepted 14 August 2019

Published 8 October 2019

Bacteria have evolved a variety of mechanisms to adapt to their physical environment. For example, in response to fluctuating environmental conditions, changes in biochemistry and gene regulation can alter bacterial shape and increase cell fitness. Cell filamentation is a commonly observed change in bacterial cell shape (1, 2) and has been described as a mechanism that enables bacteria to evade predation by the innate immune system during host infections (1).

In close proximity to surfaces, many bacteria alter their morphology and leverage cell-cell physical contact to move collectively to access new sources of nutrients and growth factors (3, 4). Referred to as “swarming,” this process is common among motile bacteria and has been connected to bacterial pathogenesis and infections (3, 4). Swarmer cells of *Salmonella enterica*, *Pseudomonas aeruginosa*, *Serratia marcescens*, and *Bacillus subtilis* have reduced susceptibility—compared to vegetative cells—to a variety of antibiotic drugs that alter protein translation, DNA transcription, and the bacterial cell membrane and cell wall (5–8). The specific biochemical and biophysical mechanisms underlying these observations are unknown.

Here, we describe physical changes in swarmer cells of the Gram-negative pathogenic bacteria *Proteus mirabilis* and *Vibrio parahaemolyticus* that have the opposite effect: they increase the susceptibility of cells to cell wall-targeting clinical antibiotics. We found that large changes in the length of *P. mirabilis* and *V. parahaemolyticus* swarmer cells are accompanied by an increase in flexibility (i.e., a reduction in cell stiffness) that enables long cells to pack together tightly and form cell-cell interactions; maximizing cell-cell interactions promotes surface motility (9). Using biophysical, biochemical, and structural techniques, we quantified changes in the structure and composition of the cell wall of *P. mirabilis* and *V. parahaemolyticus* in swarmer and vegetative cells and characterized their susceptibility to osmotic changes and cell wall-modifying antibiotics. Our results indicate that morphological changes that enable these bacteria to adapt to new physical environments come at a significant fitness cost, as cells become more susceptible to their chemical environment. In particular, changes in the composition and thickness of *P. mirabilis* and *V. parahaemolyticus* swarmer cells may make them more sensitive to osmotic changes and to cell wall-modifying antibiotics, thereby suggesting that these classes of drugs may be useful in treating infections of these bacteria (e.g., in urinary tract infections [UTIs]).

RESULTS

The bending rigidity of *P. mirabilis* and *V. parahaemolyticus* cells decreases during swarming. During surface motility, *P. mirabilis* and *V. parahaemolyticus* cells grow into swarmers that are characteristically long (10 to 100 μm) and present flagella at a high surface density that enables them to translate through viscous environments (3, 10). We found that these swarmer cells display an unusual phenotype that is rarely observed among Gram-negative bacteria: remarkable flexibility and a shape that is dynamically altered by adjacent cell motion and collisions (Fig. 1). The ability of *P. mirabilis* swarmer cells to maximize cell-cell contacts plays a role in their cooperative motility (10); our observations indicate that flexibility enables these long cells to optimize packing into multicellular structures that move cooperatively across surfaces.

Bacterial cell mechanics is generally attributed to the peptidoglycan (PG) layer of the cell wall, which has a thickness of ~ 3 to ~ 50 nm and surrounds the cytoplasmic membrane (11). Very little is known about mechanical regulation in bacteria (12–17), and we are unaware of studies connecting swarming to changes in cell mechanics. We quantified changes in swarmer-cell stiffness using cell-bending assays in a reloadable, poly(dimethylsiloxane) microfluidic system (Fig. 2; see also Fig. S1, available at <https://osf.io/hvawp>) that is related to a method developed previously (18). In bending assays, we applied a shear fluid force to multiple filamentous cells, resulting in horizontal deflection of their cell tips (Fig. 2); fitting the deflection data to a mechanical model provided us with a value of the (flexural) bending rigidity of cells (Fig. S2). After a thorough comparison of several models of variable complexity, we found our results to provide a reasonable semiquantitative estimate of bending rigidity. Introducing a

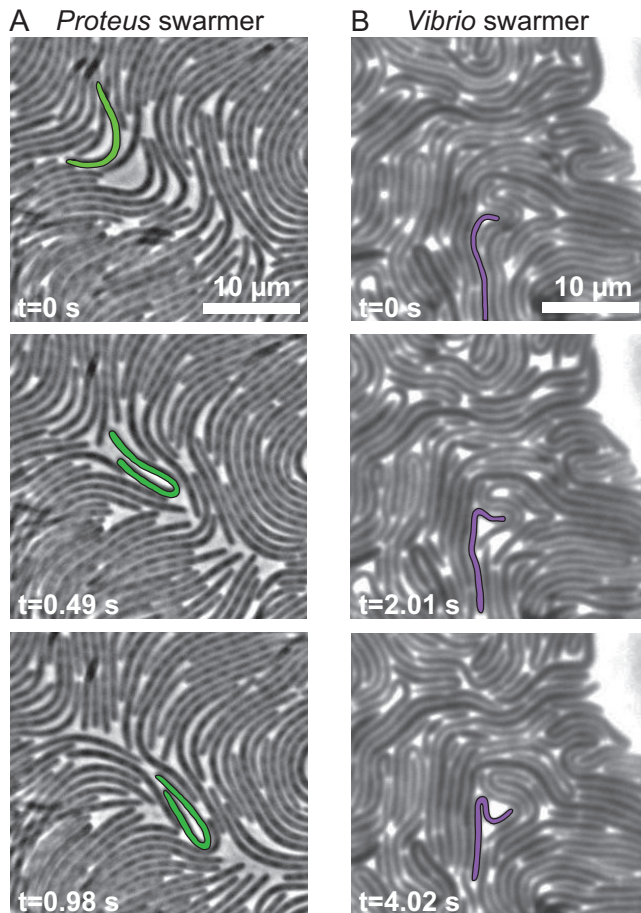


FIG 1 Images demonstrating the flexibility of *P. mirabilis* and *V. parahaemolyticus* swarmer cells. (A) Time series of *P. mirabilis* swarmer cells in a colony actively moving across the surface of a 1.5% agarose gel. A representative cell, false-colored green, had a generally straight shape at $t = 0$ s and was bent in half at $t = 0.98$ s. Most of the cells in this frame were bending during this imaging sequence. (B) A time series of *V. parahaemolyticus* swarmer cells in a colony actively moving across the surface of a 1.4% agarose gel. A representative cell (false-colored purple) had a generally straight shape at $t = 0$ s and was bent in half at $t = 4.02$ s.

reloadable mechanism enabled us to perform rapid bending measurements of *P. mirabilis* and *V. parahaemolyticus* swarmer cells after isolating them from swarm plates. Once removed from a surface, *P. mirabilis* and *V. parahaemolyticus* swarmer cells dedifferentiate, grow, and divide to form vegetative cells that resemble wild-type cells with respect to length, requiring us to rapidly perform assays with swarmer cells after their isolation from surfaces. As a point of comparison, we filamented vegetative cells of *P. mirabilis* and *V. parahaemolyticus* using aztreonam—an inhibitor of the division-specific transpeptidase PBP3—to match the length of swarmer cells ($22.2 \pm 12.5 \mu\text{m}$ and $12.4 \pm 8.2 \mu\text{m}$, respectively) and compared their bending rigidity values to those determined for swarmer cells. As a control, we measured the bending rigidity of cells of *Escherichia coli* strain MG1655, which we filamented using aztreonam, and determined the value to be $3.7 \times 10^{-20} \text{ N m}^2$ (Fig. 3); using a value for the thickness of the PG of 4 nm (19) yields a Young's modulus of 23 MPa, which is close to values that have been reported previously and supports the choice of using aztreonam to filament cells, as it apparently has no effect on the bending rigidity of cells (12, 18). We assume that the effect of aztreonam on *P. mirabilis* and *V. parahaemolyticus* cells is similar to that which we measured for *E. coli*. We found a substantial decrease in the bending rigidity of swarmer cells of both *P. mirabilis* (~26-fold) and *V. parahaemolyticus* (2.1-fold) compared to vegetative cells (Fig. 3), which is consistent with our observations of the

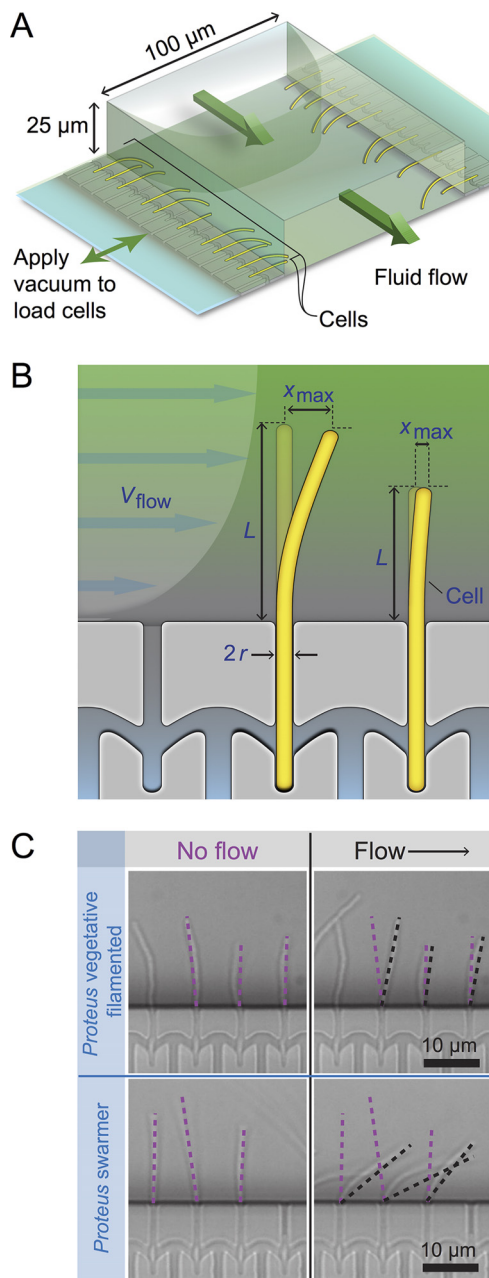


FIG 2 Using a reloadable microfluidics-based assay to determine bacterial cell stiffness. (A) Schematic of the microfluidic channel used to apply a user-defined shear force to bend filamentous or swarmer cells. Single-sided green arrows depict the flow of fluid through the central channel; the parabolic flow profile of the fluid is shown. Double-sided green arrows indicate the vacuum chamber used to load cells into side channels and to empty the device. (B) Cartoon of a flexible bacterium (left) and a stiff bacterium (right) under conditions of flow force (V_{flow}). " x_{max} " indicates the deflection of cells in the flow. $2r$ = cell diameter; L = cell length in contact with the flow force. (C) Representative images of filamentous cells of *P. mirabilis* under no-flow (left) and flow (right) conditions (top) and *P. mirabilis* swarmer cells (bottom). Purple dashed lines indicate the position of a cell tip under no-flow conditions, and black dashed lines illustrate the position after flow is applied using a gravity-fed mechanism. The arrow indicates the direction of fluid flow in the channel.

flexibility of swarming cells by microscopy. *V. parahaemolyticus* vegetative cells were remarkably flexible: ~ 154 -fold more flexible than *E. coli* cells and ~ 58 -fold more flexible than *P. mirabilis* swarmer cells (Fig. 3).

To confirm that using aztreonam to inhibit PBP3 and produce filamentous cells does not change the cross-linking density of PG at the division plane or alter cell mechanics,

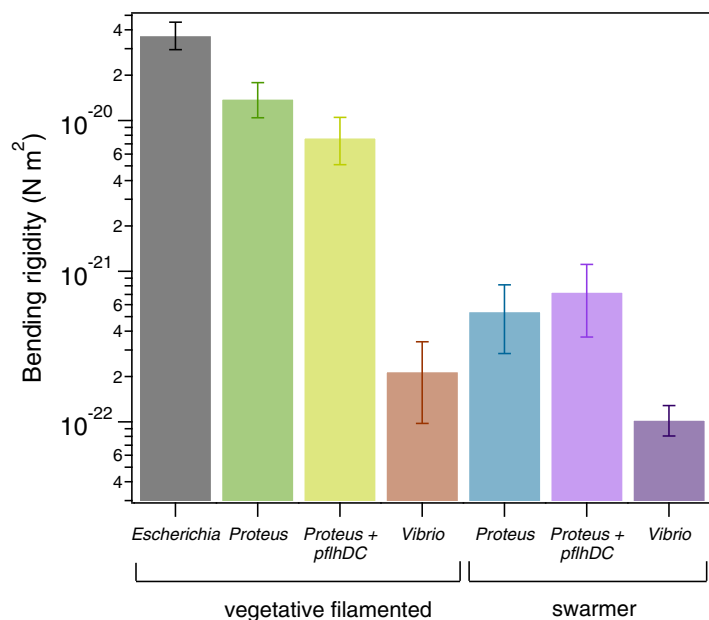


FIG 3 *P. mirabilis* and *V. parahaemolyticus* swarmer cells have a lower bending rigidity than vegetative cells. We measured the bending rigidity of *P. mirabilis* and *V. parahaemolyticus* swarmer cells and filamentous vegetative cells in a microfluidic flow assay and included measurements of vegetative *E. coli* cells. *P. mirabilis* swarmers exhibited 26-fold-lower bending rigidity than vegetative cells; *V. parahaemolyticus* swarmers were 2-fold less rigid than vegetative cells. Overexpression of FlhDC (from the plasmid-carried *pflhDC* genes) had little effect on the stiffness of *P. mirabilis* vegetative and swarmer cells. The values for each cell type represent an average of the data from two fitting models (see the supplemental material), and the bracket bars represent the upper and lower limits of the two models. More than 100 cells were used for each cell type from at least 3 independent experiments. The 95% confidence intervals associated with the fits are shown in Fig. S19. The plot has a logarithmic y-axis scale.

we compared bending rigidity values of cells treated with aztreonam and cells filamented by overexpressing SulA, a protein that prevents polymerization of the division protein FtsZ and blocks cell division. The two methods of filamenting *E. coli* cells produced similar bending rigidity values: 3.8×10^{-20} N m² (SulA) and 3.7×10^{-20} N m² (aztreonam) (Fig. S3A).

During swarming, *P. mirabilis* and *V. parahaemolyticus* cells dramatically increase their density of flagella. Since flagella are attached to these cells through a protein complex that extends through the PG (referred to as the basal body), it is possible that these structures create local defects in the PG that alter its mechanical properties. To test whether the density of flagella on swarming cells is responsible for the changes in cell mechanics that we observed, we performed bending rigidity measurements (Fig. S3B) of two K-12-derived strains of *E. coli* that have substantially different densities of flagella (Fig. S3C). Our results indicated no appreciable change in stiffness values (bending rigidity of 4.1×10^{-20} N m² at high flagellar density and 3.7×10^{-20} N m² at low flagellar density; Fig. S3B).

Overexpressing FlhDC—the heterohexameric activator that is important for swarming—in vegetative cells growing in liquid produces a phenotype that replicates many of the characteristics of swarmer cells, including increased cell length and flagellar density (20). Whether there is a relationship between FlhDC production and cell mechanics is untested. To test whether FlhDC is connected to changes in swarmer cell stiffness, we overexpressed proteins encoded by the plasmid-carried *pflhDC* genes in filamentous cells of *P. mirabilis* and measured their bending rigidity. We detected an ~1.8-fold difference in bending rigidity between the wild-type cells (1.4×10^{-20} N m²) and the *pflhDC*-containing *P. mirabilis* vegetative cells (7.8×10^{-21} N m²) and approximately equal levels of bending rigidity for the wild-type swarmer cells and *pflhDC*-containing *P. mirabilis* swarmer cells (5.5×10^{-22} and 7.4×10^{-22} N m², respectively)

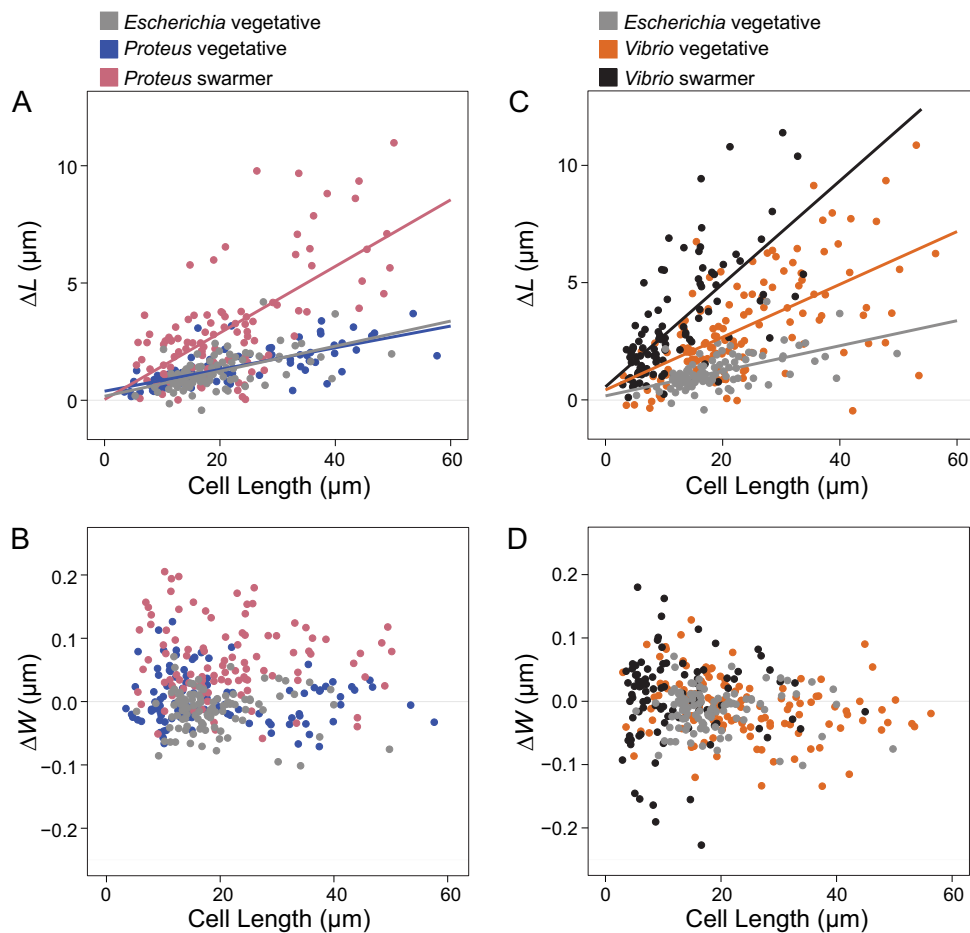


FIG 4 Swarmer cells increase in cell extension during osmotic shock. We calculated ΔL as (cell length in water – cell length in 1 M NaCl) and performed a similar calculation for ΔW , substituting cell width. Cell length indicates length prior to osmotic shock. We filamented all vegetative cells using aztreonam to grow them to lengths that were comparable with the lengths of *P. mirabilis* and *V. parahaemolyticus* swarmer cells. Lines indicate linear fits to single-cell measurements (circles) of more than 100 cells from at least 3 independent experiments. (A) *P. mirabilis* swarmer cells showed an increase in extension (ΔL) under conditions of osmotic shock compared to *E. coli* and *P. mirabilis* vegetative cells. (B) *V. parahaemolyticus* vegetative and swarmer cells showed an increase in extension (ΔL) under conditions of osmotic shock compared to *E. coli*. (C) *P. mirabilis* swarmer cells showed an increase in ΔW compared to *E. coli*; *P. mirabilis* vegetative cells displayed a slight decrease in width and increased cell length. (D) There was no observable change in ΔW of *V. parahaemolyticus* swarmer and vegetative cells.

(Fig. 3). These results indicate that FlhDC overexpression during swarming is a minor contributor to the mechanical phenotype of swarming cells; the majority of the mechanical changes that we observed arose from another regulatory pathway(s).

***P. mirabilis* and *V. parahaemolyticus* swarmer cells are more sensitive to osmotic stress than vegetative cells.** To complement the cell stiffness measurements, we also studied changes in the mechanics of swarmer cells and filamented vegetative cells by measuring their changes in length and width in response to changes in osmotic pressure, which cause cells to shrink (in a NaCl solution) and swell (in H₂O) (Fig. S4). We filamented *P. mirabilis*, *V. parahaemolyticus*, and control *E. coli* cells, using aztreonam to create a range of cell lengths that matched the lengths of *P. mirabilis* and *V. parahaemolyticus* swarmer cells. We expected that low values of bending rigidity and compositional and structural changes in PG would cause swarmer cells to elongate (in comparison to filamented, vegetative cells) in response to changes in osmotic pressure. We found that the amount of *P. mirabilis* and *V. parahaemolyticus* swarmer cell extension in response to osmotic shock was significantly greater than that seen with filamented, vegetative cells (Fig. 4). To circumvent the cellular production of osmolytes to protect cells from large changes in osmotic pressure during shock (typically pro-

duced within 1 min) (21), we used a microfluidic device to switch rapidly (<5 s) between H_2O and a NaCl solution and measured the changes in cell length that occurred before the cells adapted (Fig. S4).

Osmotic shifts produced similar changes in the length (Fig. 4A) and width (Fig. 4B) of vegetative filamented *P. mirabilis* cells compared to *E. coli* cells (Fig. 4A and B). In contrast, *V. parahaemolyticus* vegetative cells substantially increased in cell length (Fig. 4C) compared to *E. coli* cells, with no observable change in cell width (Fig. 4D). In response to osmotic downshifts (i.e., transitioning from NaCl to H_2O), *P. mirabilis* and *V. parahaemolyticus* swarmer cells dramatically increased in length (Fig. 4A and C) (and, to a lesser extent, in width for *P. mirabilis* but not for *V. parahaemolyticus*; Fig. 4B and D) compared to vegetative cells. These results suggest that the changes in *P. mirabilis* and *V. parahaemolyticus* swarmer cell stiffness made them more responsive to osmotic changes.

Changes in PG composition of *P. mirabilis* and *V. parahaemolyticus* swarmer cells. We next studied the structural and biochemical mechanisms underlying the change in the mechanical properties of swarmer cells. The connection between the structure of PG and cell mechanical properties—discovered in early antibiotic studies that revealed the penicillin binding proteins—suggested the use of PG as a starting point for these studies.

PG consists of a disaccharide building block, β -(1,4)-N-acetylmuramic acid/*N*-acetylglucosamine (MurNAc-GlcNAc), in which a pentapeptide is attached to each 3'-OH group on MurNAc. Cross-linking between adjacent pentapeptides creates a mesh-like polymeric layer, and altering its structure and composition affects cell mechanical properties (14, 15). To determine whether the PG composition of *P. mirabilis* and *V. parahaemolyticus* cells changes during swarming, we isolated PG sacculi from vegetative and swarmer cells and used ultra-high-performance liquid chromatography-mass spectrometry (UPLC-MS) to quantify their chemical composition (Fig. S5). As the PG composition of *V. parahaemolyticus* has not yet been reported, we characterized its muropeptide stem peptide using UPLC-tandem MS (UPLC-MS/MS) (Fig. S6 and S1). Similarly to *E. coli* (22) and *P. mirabilis* (23), *V. parahaemolyticus* has a PG structure like that conserved across other Gram-negative bacteria, in which the peptide stem consists of L-Ala-D-Glu-meso-diaminopimelic acid (meso-DAP)-D-Ala-D-Ala (Fig. S6).

P. mirabilis swarmer cells contained fewer monomers (MurNAc-GlcNAc), more dimers, and more anhydrous-substance-containing saccharides, which are found at the terminating end of glycan polymers, than are contained by *P. mirabilis* vegetative cells (Fig. 5A) (11). We detected no differences between swarmer and vegetative cells of *P. mirabilis* in the relative abundances of trimers (Fig. 5A). The increase in the levels of anhydrous-substance-containing saccharides that we observed in *P. mirabilis* swarmer cells was correlated with a decrease in polysaccharide length (Fig. 5B). A similar increase in the levels of anhydrous-substance-containing saccharides and decrease in the length of polysaccharides occurred in *V. parahaemolyticus* swarmer cells (Fig. 5A and B). We found no differences in cross-linking densities between vegetative and swarmer cells of either *P. mirabilis* or *V. parahaemolyticus* (Fig. 5C).

Swarmer cells have reduced PG thickness and display membrane defects. Changes in the thickness of the PG layer and structure of the cell envelope may also explain the observed decrease in swarmer cell stiffness. To identify changes in the PG thickness of swarmer cells, we isolated intact sacculi from *P. mirabilis* vegetative and swarmer cells and measured the thickness of dried sacculi using tapping-mode atomic force microscopy (AFM) (Fig. 6A). No differences in the nanoscopic appearance of the sacculi of different cells were observed by AFM (Fig. S7). The thickness of isolated, dry *P. mirabilis* swarmer cell sacculi (1.0 ± 0.2 nm) was reduced ~ 1.5 -fold compared to those of vegetative cells (1.5 ± 0.2 nm) (Fig. 6A). *V. parahaemolyticus* swarmer cells (0.6 ± 0.1 nm) exhibited a similar ~ 1.2 -fold decrease in thickness compared to vegetative cells (0.8 ± 0.2 nm). Earlier AFM measurements of isolated sacculi indicated that dehydration reduced the thickness of *Escherichia coli* PG by $\sim 2\times$, which we used to estimate the dimensions of hydrated PG from *P. mirabilis* (3.1 and 2.1 nm for vegetative

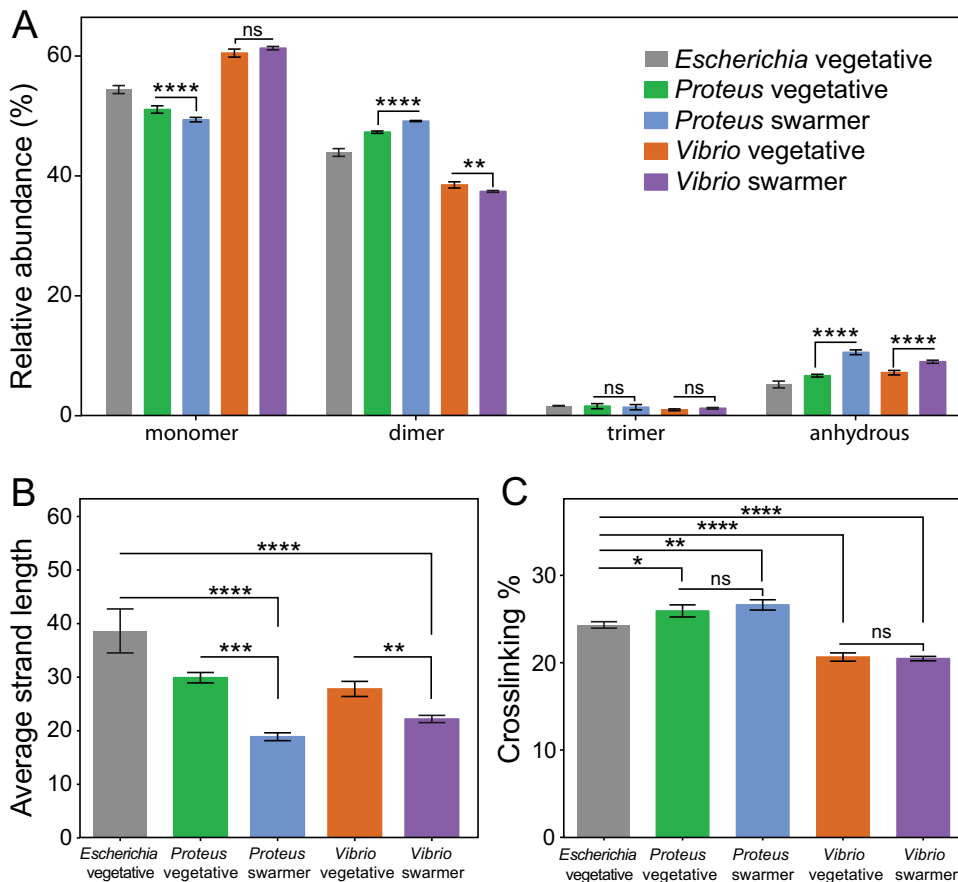


FIG 5 Alterations in the PG muropeptide composition of *P. mirabilis* and *V. parahaemolyticus* swarmer cells. (A) UPLC-MS data reveal that the muropeptide compositions of *P. mirabilis* and *V. parahaemolyticus* vegetative and swarmer cells differed slightly in the abundances of monomers, dimers, and anhydrous-substance-terminated saccharides. (B) We observed a relative increase in the amount of anhydrous-substance-containing saccharides in swarmers consistent with a decrease in polysaccharide strand length. (C) There was no change in PG cross-linking of *P. mirabilis* and *V. parahaemolyticus* vegetative and swarmer cells, although *V. parahaemolyticus* did display a lower level of cross-linking. $n = 3$ biological replicates. Error bars represent the standard deviations of the means. For (panels A to C, significance was determined via two-way analysis of variance: *, $P \leq 0.05$; **, $P \leq 0.01$; ***, $P \leq 0.001$; ****, $P \leq 0.0001$; ns, not significant ($P > 0.05$)).

and swarmer cells, respectively) and *V. parahaemolyticus* (1.7 and 1.4 nm, respectively) (24). Comparisons of PG thickness and cell-bending rigidity data suggested that the relationships between these data are approximately exponential ($R^2 = 0.9874$) (Fig. 6B).

A caveat with respect to conversions between dried and hydrated values is that they are most accurate for examples of PG that best mimic the structure and composition (e.g., cross-linking and polysaccharide composition) of the reference material: *E. coli* PG. Alterations in the polysaccharide length of PG from *P. mirabilis* and *V. parahaemolyticus* may make it more elastic and make it stretch out during drying, thereby appearing to have a thickness that is reduced compared to that of *E. coli* PG. Our control measurements of isolated, dry *E. coli* sacculi yielded a thickness value of 2.0 nm, which differs from the value of 3.0 nm published previously by Yao et al. (24), who used the same measurement technique. A difference of ~30% between these *E. coli* measurements might arise for several reasons, including variations in physical conditions that impact AFM measurements, improvement in the resolution of AFMs, and/or the precision of fitting force curves.

The relatively low range of variability (~16% to ~25%) in the values that we measured for isolated sacculi from *P. mirabilis* and *V. parahaemolyticus* cells using AFM demonstrated a consistent reduction in PG thickness for swarmer cells, suggesting that our measurements are sufficient for comparing PG from vegetative and swarming cells

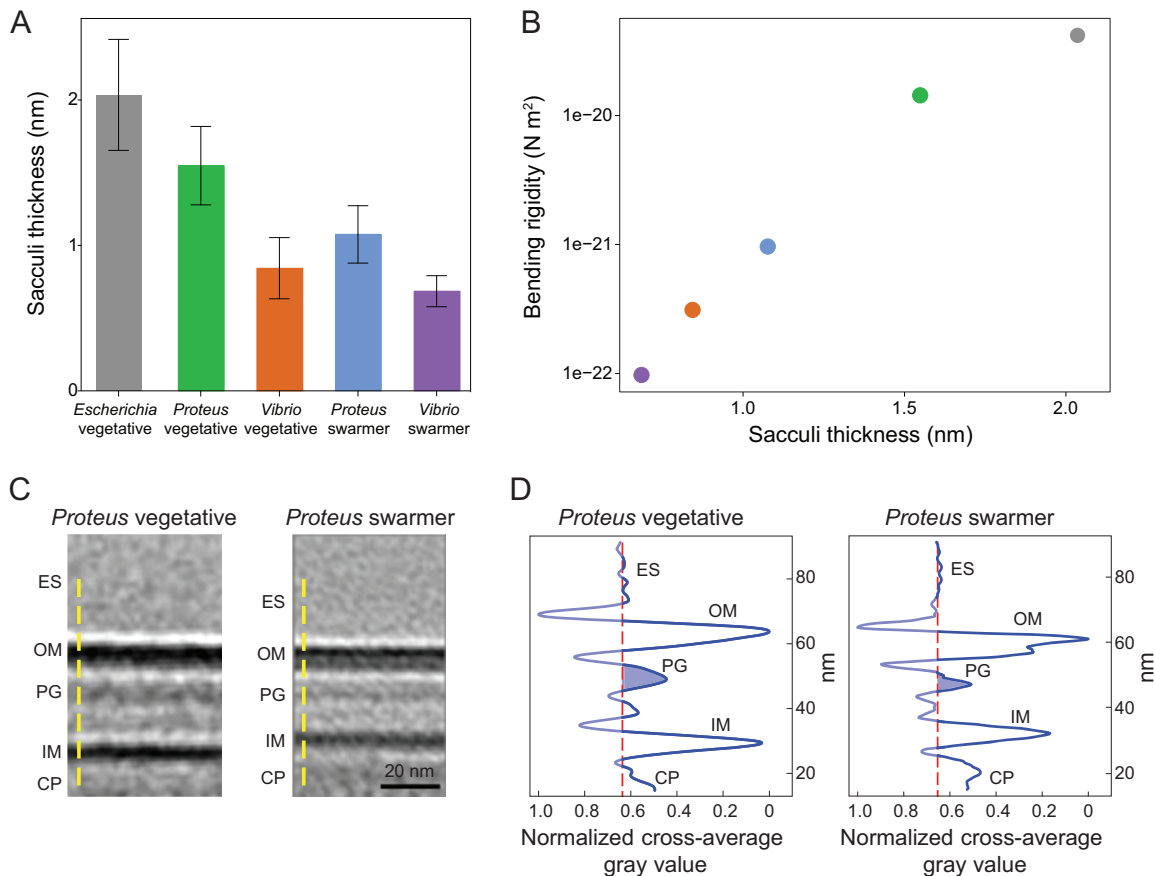


FIG 6 AFM revealed that the PG layer of *P. mirabilis* and *V. parahaemolyticus* swarmer cells is thinner than in vegetative cells, and ECT demonstrated a reduced membrane-to-membrane distance. (A) Sacculi were isolated from cells, dried, and imaged by AFM. The thickness of swarmer cell PG was reduced compared to that seen with vegetative cells. We analyzed >65 vegetative cells of *E. coli*, *P. mirabilis*, and *V. parahaemolyticus*; >65 *P. mirabilis* swarmer cells; and 7 *V. parahaemolyticus* swarmer cells. Error bars represent the standard deviations of the means. (B) Bending rigidity and cell wall thickness display an approximately exponential relationship ($R^2 = 0.9874$). (C) Subtomogram-averaged ECT volume images of the *P. mirabilis* vegetative (left) and swarmer (right) cell wall. Two central slices of subtomogram average volume images with normalized image densities are shown. Yellow dashed lines indicate the orientation used for gray-value measurements. ES, extracellular space; OM, outer membrane; PG, peptidoglycan; IM, inner membrane; CP, cytoplasm. (D) The density profile of subtomogram-averaged ECT volume images reveals reduced membrane-to-membrane distance in swarmer cells. The vertical-axis data represent normalized values corresponding to the shades of gray shown in panel C, with the darkest value equal to 0 and the lightest value equal to 1. The red dashed lines in the left and right panels denote the average value of the extracellular space represented by the shades of gray and serves as a reference for the background; the blue-shaded area indicates the thickness of the putative PG layer.

and for demonstrating a connection between PG and changes in cell mechanics. In contrast, the variability in AFM measurements and analysis makes us less comfortable with respect to comparing the absolute values of PG thickness measured in our studies to those reported for bacteria in other papers.

To complement the AFM measurements, we attempted to measure the thickness of native PG using electron cryotomography (ECT) on intact vegetative and swarmer cells (Fig. 6C and D; see also Fig. S8 and S9). Although we were unable to resolve the thickness of native PG by direct ECT measurements, we noticed that the subtomogram-averaged ECT volumes of the *P. mirabilis* cell wall (Fig. 6C) indicated that the distance between the inner and outer membranes of swarmer cells was smaller than in vegetative cells (Fig. 6C and D). *P. mirabilis* vegetative cells had a characteristically smooth membrane (Fig. S8A and B) that was similar to the presentation of the membrane found along the lateral, cylindrical walls of swarmer cells (Fig. S8C and D). In contrast, the polar regions of both *P. mirabilis* and *V. parahaemolyticus* swarmer cells had an undulating outer membrane suggestive of an altered structure (Fig. S8E and F and S9D to F), and *V. parahaemolyticus* cells had significant defects in their cell envelopes, including membrane budding, vesicle formation, and ruptured cell walls (Fig. S9D to F).

Increased susceptibility of *P. mirabilis* and *V. parahaemolyticus* swimmers to the cell wall-targeting antibiotics. Although swarming colonies of bacteria display resistance to many antibiotics (5), our experiments suggest that *P. mirabilis* and *V. parahaemolyticus* swarmer cells have changes in PG structure, composition, and properties that may increase their susceptibility to cell wall-targeting antibiotics. To determine the sensitivity of *P. mirabilis* and *V. parahaemolyticus* swimmers to the cell wall-targeting antibiotics cephalexin (which inhibits PBP3 and PBP4) (25) and penicillin G (inhibits PBP3, PBP4, and PBP6), we measured swarmer single-cell growth in the presence of the MIC of antibiotics in a microfluidic device. We determined MICs of cephalexin against vegetative cells of *E. coli* MG1655 ($1 \times \text{MIC} = 6.25 \mu\text{g/ml}$; $32 \times \text{MIC} = 200 \mu\text{g/ml}$), *P. mirabilis* ($100 \mu\text{g/ml}$), and *V. parahaemolyticus* ($50 \mu\text{g/ml}$). The MIC of penicillin G against vegetative cells of *P. mirabilis* was $12.5 \mu\text{g/ml}$. We were unable to measure MICs for these antibiotics against swarmer cells because they dedifferentiate at shorter time scales than are used for the measurements in the MIC protocol. Instead, we chose 3 h of incubation for our measurement for three key reasons: (i) swarmer cells do not dedifferentiate over this time period; (ii) a past study demonstrated that treating cells with cephalexin for 3 h was sufficient to kill $\sim 100\%$ of a population of *E. coli* cells (26); and (iii) ~ 2 h of cephalexin treatment was sufficient to observe cell lysis of *E. coli* cells measured by single-cell growth (27).

We constructed a simple microfluidic flow cell to maintain the swarming phenotype of cells during experiments and to supply cells with a source of continuously replenished fresh growth media to ensure exponential cell growth and a constant concentration of antibiotics. The channel walls consisted of the biocompatible polymer poly(dimethylsiloxane) (PDMS). Cells were in contact with the channel floor, which consisted of a layer of a 2% agarose gel. (See Fig. S12 for a cross section of the device.) We found that the survival rates of *P. mirabilis* (66%) and *V. parahaemolyticus* (64%) vegetative cells treated with $1 \times \text{MIC}$ of cephalexin were slightly higher than that of *E. coli* cells (55%) (Fig. 7A; see also Fig. S10). Treating *P. mirabilis* and *V. parahaemolyticus* swarmer cells with $1 \times \text{MIC}$ of cephalexin reduced survival to 37% and 19%, respectively (Fig. 7A; see also Fig. S10), indicating their increased susceptibility. Rates of cell survival in the presence of penicillin G were similar to those seen with cephalexin treatment (Fig. 7A). We characterized dead cells using microscopy to measure membrane blebbing, cell lysis, and changes in the refractive index of cells.

Cell wall-targeting antibiotics are most effective against actively growing cells (28, 29); therefore, increases in growth rates reduce cell survival. To determine whether a growth rate phenotype explains our observations, we normalized data for cell length and were unable to detect a change in the growth rate of swarmer cells under conditions of treatment with these two antibiotics (Fig. S11). We measured the mean survival time of cells (the amount of time elapsed after treatment with drugs before cell death) for *P. mirabilis* and *V. parahaemolyticus* swarmer cells treated with cephalexin and penicillin G (Fig. 7B) and found that the survival time for these swarmer cells was lower than that for vegetative cells (Fig. 7B), which is consistent with alterations in the cell wall.

DISCUSSION

P. mirabilis is commonly associated with complicated urinary tract infections and increased mortality in cases of bacteremia (30). Swarming is hypothesized to enable *P. mirabilis* cell movement from the ureter to the kidney; in support of this hypothesis, swarming-deficient mutants have lower rates of host infection (31). We found that during swarming, *P. mirabilis* and *V. parahaemolyticus* cells become more flexible due to changes in the thickness and composition of the PG. Although we were unable to precisely measure the thickness of isolated PG, the decrease in the distance between the inner and outer membranes of swimmers may reflect a reduction in PG thickness. Several recent studies suggested how changes in the cell wall influence cell stiffness. A recent study revealed the connection between changes in the biochemical regulation of D-Ala-D-Ala and *Pseudomonas aeruginosa* cell stiffness in cells in which this biochem-

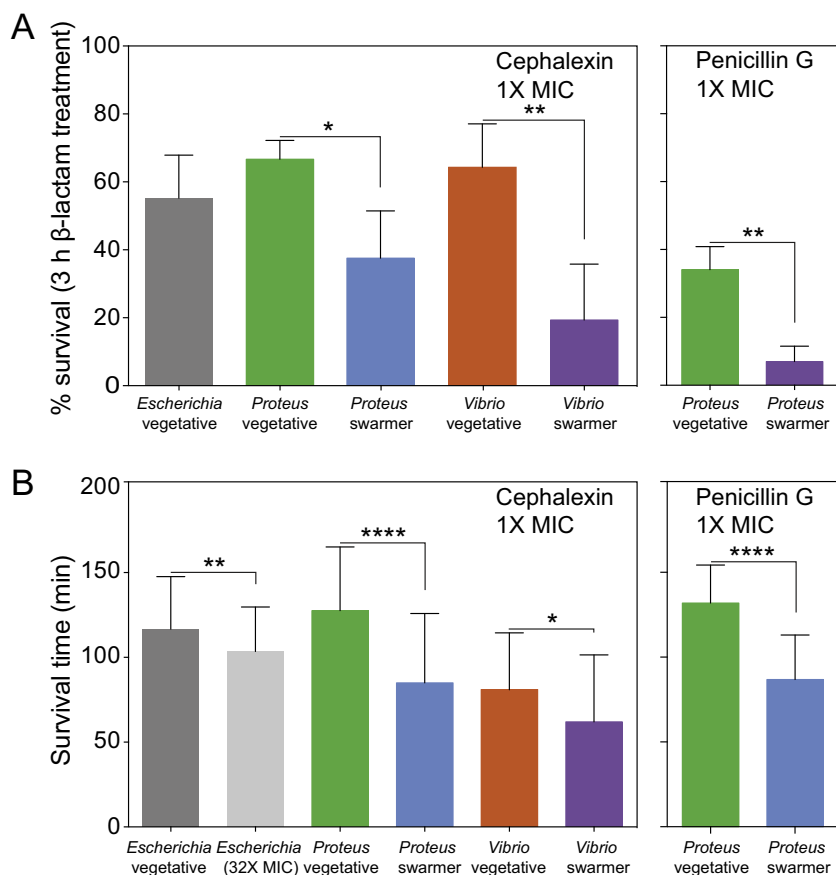


FIG 7 Swarmer cells are more susceptible to antibiotics that target the cell wall than vegetative cells. (A) Survival of cells treated with 1× MIC of cephalixin after 3 h of incubation. We define percent survival as follows: $(\text{cell count}_{\text{no lysis}} / \text{cell count}_{\text{total}}) \times 100$. *P. mirabilis* and *V. parahaemolyticus* swarmer cells exhibited levels of survival that were decreased (~30%) compared to those seen with vegetative cells ($n = \geq 90$ cells from at least two independent experiments). A similar decrease occurred when *P. mirabilis* was treated with penicillin G ($n = \geq 77$ cells from at least two independent experiments). Error bars represent the standard deviations of the means. (B) After exposure to cephalixin or penicillin G, the survival time of *P. mirabilis* and *V. parahaemolyticus* swarmers was ~2-fold to ~3-fold lower than that of vegetative cells. Survival time was determined for ≥ 49 cells that lysed from at least 2 independent experiments. The statistical significance of the data presented in panels A and B was determined using a two-tailed t test. *, $P \leq 0.05$; **, $P \leq 0.01$; ***, $P \leq 0.0001$.

ical machinery is altered (32). The current study and the *P. aeruginosa* paper (32) demonstrate that it is still difficult to quantitatively understand the scaling between the magnitude of the biochemical changes in cells and changes in cell stiffness. The range of techniques now available for quantitatively measuring single-cell stiffness will enable the development of this relationship.

We found that *P. mirabilis* and *V. parahaemolyticus* swarmer cells were more susceptible to large changes in cell length than vegetative cells during osmotic shift experiments. Although these changes are consistent with what would be expected from a reduction in PG thickness in swarming cells, they are also relevant to other cell wall changes. We also observed that the length of polysaccharides was reduced in swarming cells, which would not obviously lead to large changes in cell elongation during osmotic shifts if the organization of PG in these cells follows what is known about the structure of PG in *E. coli* cells (33): polysaccharides reported to be arranged circumferentially around cells with the peptide cross-links oriented parallel to the long axis of cells. Instead, we expect that a decrease in polysaccharide length would make swarmer cells more prone to changes in diameter. *P. mirabilis* swarmer cells appear to increase in diameter during osmotic shifts (with no change occurring for vegetative

cells); however, the data are noisy and do not accurately fit with standard models. We were unable to observe a trend with *V. parahaemolyticus* swarmer cells (Fig. 5).

Another recent study demonstrated the role of the outer membrane in the cell stiffness of Gram-negative bacteria (34). Chemical and genetic changes in the outer membrane increased the deformation of the cell envelope in response to stretching, bending, and indentation forces and increased the amount of cell lysis arising during osmotic shock. It is possible that the morphological changes in swarmer cell membranes that we observed during ECT experiments indicate membrane perturbations that contribute significantly to changes in cell stiffness. Swarming in *Proteus* and *Vibrio* is well known to occur in parallel with the secretion of lipopolysaccharides (3, 4), the source of which is presumably the outer membrane of these bacteria, which may alter cell stiffness.

This paper reports for the first time the ability of bacteria to modulate their cell stiffness (beyond L-forms). This phenotype (i.e., greater flexibility) presumably conveys an adaptive advantage for cells that is supported by observations from many laboratories reporting that the motility of communities of swarmer cells is enhanced when cell-cell contacts are increased. The adaptive advantage of swarming in *P. mirabilis* and *V. parahaemolyticus*, however, appears to be offset by a decrease in their fitness, as cells become more sensitive to osmotic changes and cell wall-targeting antibiotics, thereby creating an “Achilles heel” with respect to targeting this phenotype in infectious diseases. This report highlights the plasticity of bacteria (1), the continuing need for methods of evaluating chemotherapies that measure efficacy against cells in a physiological state relevant to specific infections, and the reconsideration of cell wall-targeting antibiotics for treating UTIs and other infections in which *P. mirabilis* and *V. parahaemolyticus* may be present.

MATERIALS AND METHODS

Bacterial strains and cell culture. *P. mirabilis* strain HI4320, *V. parahaemolyticus* LM5674, *Escherichia coli* MG1655 (CGSC catalog no. 6300), and plasmids *pflhDC* (10) and *psuA* (18) were used for the experiments reported in this paper. *P. mirabilis* was grown in PLB nutrient medium, consisting of 1% (wt/vol) peptone, 0.5% (wt/vol) yeast extract, and 1% (wt/vol) NaCl. *V. parahaemolyticus* was grown in nutrient medium (HI medium), consisting of 2.5% (wt/vol) heart infusion broth and 2.5% (wt/vol) NaCl. *E. coli* was grown in lysogeny broth (LB), consisting of 1% (wt/vol) tryptone, 0.5% (wt/vol) yeast extract, and 1% (wt/vol) NaCl. All strains were grown at 30°C with shaking at 200 rpm.

Immunostaining of flagella on *E. coli* cells to determine flagellar surface density. As a control to determine the influence of the surface density of bacterial flagella on measurements of bending rigidity, we imaged two *E. coli* MG1655 strains with different densities of flagella using a polyclonal flagellin antibody and an immunostaining procedure for visualization of flagella (10).

Calculating vegetative and swarmer cell division times. We prepared vegetative cells by diluting an overnight culture 1:200 in fresh medium and grew the cells at 30°C with shaking at 200 rpm to an optical density (OD; $\lambda = 600$ nm) of 0.6. We prepared swarmer cells as described previously (10). We monitored the growth of *P. mirabilis*, *V. parahaemolyticus*, and *E. coli* vegetative cells over 120 min at 30°C in the microfluidic flow chamber device described in the next section. We performed a similar experiment with *P. mirabilis* and *V. parahaemolyticus* swarmers growing over 65 min at 30°C to determine the amount of time that elapsed before the cells divided. We collected images of cells at 1-min intervals and determined the division time for a maximum of 10 generations (for vegetative cells) and 4 division events (for swarmer cells).

Measuring the sensitivity of cells to osmotic shock in a microfluidic device. We prepared filamentous vegetative cells of *P. mirabilis* and *V. parahaemolyticus* by diluting an overnight culture of cells 1:200 into fresh medium. We then grew cultures at 30°C with shaking for 1 h, added aztreonam (MP Biomedicals) to reach a final concentration of 10 μ g/ml, and grew the cells for an additional 70 min. Swarmer cells were prepared as described previously (10). To maximize the number of cells attached to a surface in the microfluidic device (flow chamber construction described below), we concentrated cells to an OD₆₀₀ of 8 in 100 μ l of liquid nutrient medium.

We prepared the microfluidic device for experiments by flowing 10 μ l of undiluted Cell-Tak (Corning) into the device and incubating it for 10 min at 25°C. Next, we flowed 20 μ l of a suspension of cells (OD₆₀₀ of 8) through the device and then repeated the procedure with another 20- μ l aliquot of cell suspension. To aid the adherence of the highly motile swarmer cells to the Cell-Tak-coated surface, we centrifuged the device for 5 min at 300 \times g in a centrifuge (Beckman Coulter) equipped with a swinging bucket rotor.

For osmotic shock experiments, we filled separate 1-ml syringes (BD) with a solution of UltraPure distilled water (Invitrogen) or a 1 M concentration of a NaCl solution prepared in double-distilled water (ddH₂O) and connected the syringes using a three-way valve. We mounted the microfluidic device on a TE2000-E inverted microscope and imaged cells in the chamber at 25°C (decreasing the temperature resulted in reduced growth and cell division). Prior to the osmotic shock step, we flowed 200 μ l of fresh

liquid media (PLB for *P. mirabilis*, LB for *E. coli*, and HI for *V. parahaemolyticus*) through the device to remove cells that were not adhered to the channel surface. While imaging, we flowed a 1 M NaCl solution through the channel and observed cell plasmolysis, immediately after which we flowed ddH₂O through the channel and observed cells elongating. We collected images of hundreds of single cells after exposing them to three conditions: (i) isotonic culture (PLB, LB, HI); (ii) hypertonic shock (1 M NaCl); and (iii) hypotonic shock (ddH₂O).

To determine changes in cell size and width, we extracted individual cell contours from the images taken for each treatment using MATLAB 2014a (MathWorks) and used MicrobeTracker (35) to determine cell lengths (L) and widths (W). From these measurements we calculated ΔL ($L_{\text{hypotonic}} - L_{\text{hypertonic}}$) and ΔW ($W_{\text{hypotonic}} - W_{\text{hypertonic}}$) for vegetative and swarmer cells of *P. mirabilis* and *V. parahaemolyticus*.

Determining the MIC of vegetative cells of *P. mirabilis* and *V. parahaemolyticus*. We used the microdilution protocol (36) to determine the MIC of cephalixin in accordance with Clinical and Laboratory Standards Institute guidelines. Briefly, we added 400 $\mu\text{g/ml}$ of cephalixin (BP Biomedicals) or penicillin G (BP Biomedicals) to the first well of a 96-well microplate (Nunc) and diluted these antibiotics 2-fold across adjacent wells (wells 1 to 11; well 12 was a no-drug control). We determined the MIC after 16 h of growth at 30°C with shaking by identifying by visual inspection the lowest concentration of cephalixin and penicillin G that inhibited cell growth. The MIC was determined from three replicate plates. We determined the MIC of cephalixin against *E. coli* MG1655 ($1 \times \text{MIC} = 6.25 \mu\text{g/ml}$; $32 \times \text{MIC} = 200 \mu\text{g/ml}$), *P. mirabilis* (100 $\mu\text{g/ml}$), and *V. parahaemolyticus* (50 $\mu\text{g/ml}$). The MIC of penicillin G against *P. mirabilis* was 12.5 $\mu\text{g/ml}$.

Antibiotic treatment of vegetative and swarmer cells and measurement of their growth in a microfluidic device. We prepared vegetative and swarmer cells of *P. mirabilis* and *V. parahaemolyticus* as described above. Prior to use, we diluted cells 1:100 in fresh medium to a cell density that enabled us to image many individual cells simultaneously in the microfluidic device described in the section above.

To prepare the microfluidic device for monitoring growth, we applied a 250- μm -thick layer of PDMS prepolymer to the surface of cover glass (Fisherbrand) (no. 1.5; 35 by 50 mm) by the use of a Spin Coater (Laurell Technologies) and polymerized the polymer overnight at 60°C. We subsequently removed a 6-mm-by-4-mm rectangle of PDMS from the center of the cover glass using a scalpel. We applied transparent tape to both sides of this rectangular well and pipetted 100 μl of media containing a 2% (wt/vol) solution of UltraPure agarose (Invitrogen) into the well. We placed a cover glass (Fisherbrand) (no. 1.5; 22 by 30 mm) on top of the liquid agarose (to flatten the agarose surface), pressed the cover glass against the transparent tape, and solidified the agarose at 25°C. Next, we removed the no. 1.5 cover glass and tape and any residual agarose from the PDMS surface. We pipetted 2 μl of a suspension of cells on the agarose pad surface, waited until the excess liquid had evaporated or been absorbed by the agarose, carefully removed the agarose layer, inverted it, and placed it back into the well such that the cells were positioned between the agarose surface and the cover glass. We placed the PDMS flow chamber used in the construction of the osmotic shock microfluidic device on the PDMS-coated cover glass and aligned it such that the agarose pad was centered in the flow channel (see Fig. S12, available at <https://osf.io/hvawp>).

For antibiotic treatment of cells in the microfluidic cell growth device, we filled a 6-ml syringe (Norm-Ject) with cephalixin or penicillin G at a concentration corresponding to $1 \times \text{MIC}$ dissolved in nutrient medium. We supplied a constant flow of 20 $\mu\text{l/min}$ to the device using a syringe pump (Harvard Apparatus) and monitored the growth of individual cells during antibiotic exposure using a TE2000-E inverted microscope. The stage and objective heater were maintained at 30°C. Images were collected every 1 min for 3 h.

Due to the aberrant shape of cells treated with cephalixin and penicillin G (Fig. S10), we were unable to use an automated script (e.g., MicrobeTracker) to determine cell death. Instead, we visually determined the time of death for individual cells when they exhibited three phenotypes that collectively indicate cell death: blebbing (membrane swelling), lysis (bleb rupture), and disappearance of cells in phase-contrast microscopy (loss of cytoplasmic material).

Determining cell growth rates in the presence of antibiotics. We prepared vegetative and swarmer cells of *P. mirabilis* and *V. parahaemolyticus* as described above. We monitored individual cell growth at 30°C in the presence of $1 \times \text{MIC}$ of cephalixin and penicillin G in our microfluidic growth device (described above) by collecting an image every 1 min for 15 min. To calculate the growth rate, we first extracted individual cell contours at each time point using MicrobeTracker and determined cell length. To take into account the differences in starting length between *P. mirabilis* and *V. parahaemolyticus* cells, we normalized the change in length to the initial cell length ($\Delta L/L_0$) at each time point. To determine the growth rate for individual cells, we fitted their relative length over time to an exponential function using GraphPad Prism 6.0 (GraphPad Software).

Measuring cell envelope architecture and peptidoglycan thickness using electron cryotomography. We prepared vegetative and swarmer cells of *P. mirabilis* and *V. parahaemolyticus* and concentrated them to an OD₆₀₀ of 10. For ECT, we mixed vegetative and swarmer cells with bovine serum albumin-treated 10-nm-diameter gold particles that served as fiducial markers, applied them to electron microscopy grids, and subjected them to plunge-freezing in a mixture of liquid ethane and propane, as described previously (37). Grids were stored in liquid nitrogen until imaging was performed.

We acquired images on a 300-KeV Polara transmission electron microscope (FEI) with a GIF energy filter (Gatan) and a K2 Summit direct detector (Gatan). We collected tilt series from -60° to $+60^\circ$ with 1° increments using UCSFotomo software with a defocus of $-10 \mu\text{m}$ and a total dosage of $190 \text{ e}^-/\text{\AA}^2$ (38) at a magnification of $\times 27,500$. Tomograms were calculated using IMOD software (39).

For subtomogram averaging, smooth and flat membrane regions were chosen by eye; a volume of 40-by-70-by-12 voxels (62 nm by 109 nm by 19 nm) was centered using the outer membrane and extracted. We aligned 38 extracted “membrane fragments” from four *P. mirabilis* vegetative cells and 42 fragments from nine *P. mirabilis* swarmer cells and averaged them in PEET (40). The densities from two averaged membranes were scaled to match each other using IMOD (39), cross-averaged density profiles were measured using ImageJ 1.50c (41), and figures were generated in OriginPro (OriginLab).

Determining the thickness of *P. mirabilis* and *V. parahaemolyticus* sacculi (isolated peptidoglycan) by atomic force microscopy (AFM) in ambient conditions. We isolated *P. mirabilis* and *V. parahaemolyticus* swarmer cells, concentrated them at $800 \times g$ for 10 min, removed the supernatant, subjected the cell pellet to flash-freezing in liquid nitrogen, and stored it at -80°C . Swarmer cell pellets were thawed at 4°C and pooled for isolation of sacculi (intact peptidoglycan). To increase the efficiency of cell lysis prior to isolating sacculi, we resuspended vegetative and swarmer cell pellets in 3 ml of cold $1 \times$ phosphate-buffered saline (Thermo Scientific) and then lysed cells with a tip sonicator (Qsonica) for ~ 10 s at a power setting of 75%. We confirmed cell lysis using optical microscopy. We isolated sonicated cells, resuspended sacculi in $20 \mu\text{l}$ of ddH_2O (*V. parahaemolyticus* swarmer) or $200 \mu\text{l}$ of ddH_2O (all other cells), immediately subjected the sacculi to flash-freezing in liquid nitrogen, and stored them at -80°C .

To prepare sacculi for AFM, we transferred $10 \mu\text{l}$ of sacculi thawed at 4°C to a new microcentrifuge tube placed in a bath sonicator (Branson) that was cooled with ice for 10 min to aid in the dispersal of sacculi without affecting the sacculus architecture (42). After sonication, we pipetted $10 \mu\text{l}$ of the sacculi onto freshly cleaved mica (Ted Pella), dried the mica under nitrogen gas, washed it three times with 1 ml of ddH_2O (filtered through a $0.2\text{-}\mu\text{m}$ -pore-diameter filter [Corning]), dried the sacculi under nitrogen gas, and performed imaging immediately after preparation.

We performed AFM using a Catalyst AFM (Bruker) operating in tapping mode under ambient conditions (air) with an aluminum reflex-coated silicon AFM probe (Ted Pella; $k = 40 \text{ N/m}$). Before imaging, AFM probes were autotuned using Nanoscope 8.15 (Bruker). We collected all images at high resolution (512 by 512 pixels) with a scan speed of 1 Hz and analyzed images using NanoScope Analysis 1.4 (Bruker). Prior to determining the thickness of the sacculi, we flattened (0th order) all images to remove variations in surface thickness. Thickness was determined perpendicularly to the long axis; we avoided surface debris, folds in the sacculi, and trapped material in sacculi (Fig. S7).

Determining the composition of peptidoglycan in *P. mirabilis* and *V. parahaemolyticus* vegetative and swarmer cells using ultra-high-performance liquid chromatography/mass spectrometry (UPLC/MS). We prepared vegetative and swarmer cells of *P. mirabilis* and *V. parahaemolyticus* as described above. To purify peptidoglycan for UPLC/MS, we carried out a previously reported isolation technique for Gram-negative bacteria (43) with the following modifications. Briefly, after trypsin (Sigma) inactivation, we incubated the sacculi in 1 M HCl solution (Fluka) for 4 h at 37°C to remove any O-acetylation from the peptidoglycan, which is present in *P. mirabilis* (23). Then, the sacculi were washed three times in ddH_2O , resuspended in 500 mM boric acid (Sigma) [pH 9] to an OD_{600} of 3, and mixed with 1/10 the volume of mutanolysin (Sigma). The sample was incubated 16 h at 37°C with shaking at 200 rpm. The next day, the samples were centrifuged for 10 min at $9,500 \times g$, pelleting the remaining insoluble material. The supernatant was removed and put into a glass vial. To reduce the isolated muropeptide fragments, we added $50 \mu\text{l}$ of $20 \mu\text{g/ml}$ sodium borohydride (Sigma)– 500 mM boric acid (pH 9) and incubated the mixture for 30 min at 25°C . We adjusted the pH of the solution to 2 to 3 by adding 50% phosphoric acid (Fluka) and then filtered the muropeptide solution through a Durapore polyvinylidene fluoride filter (Millex) ($0.22\text{-}\mu\text{m}$ pores) into a clean vial. Vials were immediately stored at -80°C until use within 1 week of muropeptide isolation.

For UPLC/MS, we injected $7.5 \mu\text{l}$ of purified muropeptides into a Cortecs C_{18} column (Waters) (2.1 by 100 mm) packed with $1.6\text{-}\mu\text{m}$ -diameter particles and equipped with a Cortecs C_{18} guard column (Waters). The column temperature was maintained at 52°C using an Acquity standard flow UPLC system equipped with an inline photodiode array (Waters). For muropeptide separation by UPLC, we used solvent A (Optima liquid chromatography-mass spectrometry [LCMS]-grade water with 0.05% trifluoroacetic acid) and solvent B (30% [vol/vol] Optima LCMS-grade methanol, Optima LCMS-grade water, and 0.05% trifluoroacetic acid) (Fisher Scientific). Muropeptides were eluted from the column with a gradient of increasing levels of solvent B (1-min hold at 1% solvent B, ramp to 99% solvent B over 59 min, hold at 99% solvent B for 5 min, followed by a decrease to 1% solvent B over 1.5 min and then a hold at 1% solvent B for 4.5 min) at a flow rate of 0.2 ml/min . We analyzed the eluent from the column using a Bruker Maxis ultra-high-resolution time-of-flight 4G mass spectrometer (Bruker Daltonic) with either an MS method or a data-dependent, top 3 MS/MS method. For both methods, capillary voltage was set to $4,100 \text{ V}$, the nebulizer pressure was 2.0 bar , and the drying gas was set to 6.0 liters/min at 220°C . Muropeptides were detected at a λ level of 205 nm by MS.

We determined the peptidoglycan composition of *E. coli*, *P. mirabilis*, and *V. parahaemolyticus* vegetative and swarmer cells by comparing MS/MS fragmentation patterns using DataAnalysis version 4.2 (Bruker) (Fig. S6). Muropeptides were identified according to mass values using DataAnalysis 4.2. We calculated muropeptide masses using ChemDraw 14.0 (CambridgeSoft) (see Table S1, available at <https://osf.io/hvawp>). We quantified the corresponding UV ($\lambda = 205$) absorbing peaks (Fig. S5) identified by MS (Bruker), from which we calculated the peptidoglycan cross-linking density and strand length (44) for each species. Statistical significance was determined using GraphPad Prism 6.0.

Fabrication of microfluidic devices for measuring cell bending and cell growth. Masters for the cell-bending device and the cell growth/osmotic shock device were fabricated on separate 3-in^2 silicon wafers using SU8 photoresist that was exposed on a Heidelberg μPG101 mask writer (Heidelberg Instruments, Heidelberg, Germany) and developed. The bending device (Fig. S1) used was a 2-layer

device. The first SU8 layer consisted of $\sim 1\text{-}\mu\text{m}$ -tall channels for capturing cells. The wafer was then coated with the second SU8 layer ($\sim 25\text{ }\mu\text{m}$ tall), which formed a central flow channel. The flow chamber (Fig. S12) consisted of a single channel with a length of 10 mm, a width of 5 mm, and a height of $50\text{ }\mu\text{m}$. The volume of the flow chamber was $\sim 10\text{ }\mu\text{l}$. After developing the masters for both devices, we used the masters to emboss layers of poly(dimethylsiloxane) (PDMS), punched holes for inlets and outlets, and cleaned the surfaces with tape. If the device was attached to a glass coverslip, it was treated with oxygen plasma and immediately sealed against a plasma-treated no. 1.5 cover glass (Fisherbrand) (24 by 50 mm) to form a permanent seal.

Measuring the bending rigidity of *P. mirabilis*, *V. parahaemolyticus*, and *E. coli* cells. We used streak velocimetry to determine the profile of fluid flow rates in the central channel of the microfluidic device driven by gravity flow. We added fluorescently labeled $0.22\text{-}\mu\text{m}$ -diameter microspheres (Polysciences) diluted $\sim 1:10,000$ in ddH₂O containing 0.01% Brij 35 (Sigma) to the microfluidic channel and collected videos of the fluorescent beads moving through the channel at focal planes $2\text{ }\mu\text{m}$ apart. We analyzed the movies with custom-written code in Igor Pro 6.37 (WaveMetrics). Briefly, we applied a Gaussian blur and threshold to each frame and used the thresholded image to establish a region that was fitted to a function based on a two-dimensional (2D) Gaussian function. We used the image exposure time and the length of the streaks—taking into account the size of the microspheres—to calculate microsphere velocity. We mapped the velocity profile within the channel by analyzing several hundred microspheres. We binned the velocity data into a 3D matrix and fitted it to a Poiseuille function, letting the velocity coefficient, height, and width float. The calculated velocity coefficient was used as an input to the cell-bending fitting function.

The system for gravity flow pumping (Fig. S13) consisted of two 6-ml syringes (Norm-Ject), one 60-ml syringe (BD), one 1-ml syringe (Norm-Ject), a ruler, and a VC-6 channel valve controller (Warner Instruments) connected to a VC-8 minivalve system (Warner Instruments) that drives a three-way solenoid valve (The Lee Company). Syringe no. 1 (6 ml) was mounted to an immobile post, positioned 40 cm above the table surface; this syringe was used to load cells. Syringe no. 2 (6 ml) was positioned 75 cm above the table surface, was connected to a stage that could be raised and lowered vertically, and was used to apply flow force in the device. Syringe no. 3 (60 ml) was mounted to an immobile post, was positioned 75 cm above the surface of the table, and was used to apply an opposing flow force at the device outlet and to collect spent media/cells. We attached two-way valves, a blunt-end needle, and tubing to each syringe, including syringe no. 4 (1 ml). We joined the two 6-ml syringes using a Y-junction connector that led to the VC-8 minivalve system inlet. The outlet of the valve system was connected to the microfluidic system. A ruler on an immobile post indicated the zero position (no pressure).

For cell-bending experiments, we prepared filamentous vegetative cells and swarmer cells of *P. mirabilis* and *V. parahaemolyticus*; cells were normalized to an optical density (OD; $\lambda = 600\text{ nm}$) of 1. Prior to starting a measurement, syringes 1 and 2 were flushed with ddH₂O and fresh medium. Syringe 2 was filled with 4 ml of medium, syringe 3 was filled with 30 ml of ddH₂O, and syringe 4 was filled with 0.8 ml of ddH₂O. We added cells to syringe 1 and allowed them to flow through the tubing until they reached the device outlet. To load the cells into the side channels of the device (from the central channel), we applied a suction force using the 1-ml syringe. After the side channels were loaded with cells, we adjusted the height of syringe 2 until no flow occurred in the device. Syringe 2 was then raised 7 cm from the no-flow position (a height of 0 cm). We collected images of cells in the channel when syringe 2 was at positions 0 cm and 7 cm using a Zeiss Axiovert 100 inverted microscope (Zeiss) equipped with an iXon3 charge-coupled-device (CCD) camera (Andor), a $63\times$ Plan-Apochromat oil objective (Zeiss), and Micro-Manager 1.4.16. After collecting cell-bending deflections for all loaded cells, we expelled cells from the side channels, allowed the liquid to flow through the device for 15 s, and reloaded the side channels with new cells.

We analyzed images to determine cell deflection under flow conditions using custom image analysis software written in Igor Pro 6.37. The cell-bending model (see the supplemental material) is a differential equation that lacks an analytical solution and thus requires calculation of a numerical solution. To determine the bending rigidity of cells, we wrote custom fitting code in Igor Pro 6.37 that uses a variety of input parameters, including channel dimensions, fluid velocity, bending rigidity of the cell, cell radius, and cell length. The function numerically calculates the maximum deflection based on our model. This function is integrated into a fitting algorithm to find a least-squares solution to a data set of maximum deflections versus cell lengths with bending rigidity as the fitting parameter.

Our model for bending a cell under flow conditions is based on the mechanics model of a suspended rod or cantilever bending under its own weight (see "Derivations" in the supplemental material). Our experimental system was similar to that of Amir et al. (18). Although the laminar flow is perpendicular to the long axis of cells in this system, the lateral deformations of cells that we measured were substantially larger (in our case, as large as $10\text{ }\mu\text{m}$ compared to the value of $<1\text{ }\mu\text{m}$ reported previously by Amir et al. [18]). For this reason, many of the assumptions in the model presented by Amir et al. are not valid for our data set. The model that we developed to extract the bending rigidity of the bacterium takes into account the shape of the laminar flow profile, the angle of the cell against the flow profile, and the arc length of the cell (longer cells tend to fold over and do not penetrate as deeply into the flow profile). Additional data and mathematical derivations are described in the supplemental material.

Supplemental material can be found at OSF (<https://osf.io/hvawp>).

ACKNOWLEDGMENTS

We thank Linda McCarter for *V. parahaemolyticus* LM5674, Suckjoon Jun for plasmid *psuA*, Cameron Scarlett and Molly Pellitteri-Hahn for mass spectrometry support, and Julie Last for technical assistance with AFM measurements.

This research was supported by the Bill and Melinda Gates Foundation (grant OPP1068092), NIH grant 1DP2OD008735-01, National Science Foundation (NSF) grant DMR-1121288, a Mao Wisconsin Distinguished Graduate Fellowship (to M.R.), an NSF postdoctoral fellowship (no. 1202622 to P.M.O.), and the Howard Hughes Medical Institute.

REFERENCES

- Justice SS, Hunstad DA, Cegelski L, Hultgren SJ. 2008. Morphological plasticity as a bacterial survival strategy. *Nat Rev Microbiol* 6:162–168. <https://doi.org/10.1038/nrmicro1820>.
- Rajendram M, Zhang L, Reynolds BJ, Auer GK, Tuson HH, Ngo KV, Cox MM, Yethiraj A, Cui Q, Weibel DB. 2015. Anionic phospholipids stabilize RecA filament bundles in *Escherichia coli*. *Mol Cell* 60:374–384. <https://doi.org/10.1016/j.molcel.2015.09.009>.
- Copeland MF, Weibel DB. 2009. Bacterial swarming: a model system for studying dynamic self-assembly. *Soft Matter* 5:1174–1187. <https://doi.org/10.1039/B812146J>.
- Kearns DB. 2010. A field guide to bacterial swarming motility. *Nat Rev Microbiol* 8:634–644. <https://doi.org/10.1038/nrmicro2405>.
- Butler MT, Wang Q, Harshey RM. 2010. Cell density and mobility protect swarming bacteria against antibiotics. *Proc Natl Acad Sci U S A* 107:3776–3781. <https://doi.org/10.1073/pnas.0910934107>.
- Kim W, Killam T, Sood V, Surette MG. 2003. Swarm-cell differentiation in *Salmonella enterica* serovar typhimurium results in elevated resistance to multiple antibiotics. *J Bacteriol* 185:3111–3117. <https://doi.org/10.1128/jb.185.10.3111-3117.2003>.
- Overhage J, Bains M, Brazas MD, Hancock RE. 2008. Swarming of *Pseudomonas aeruginosa* is a complex adaptation leading to increased production of virulence factors and antibiotic resistance. *J Bacteriol* 190:2671–2679. <https://doi.org/10.1128/JB.01659-07>.
- Lai S, Tremblay J, Deziel E. 2009. Swarming motility: a multicellular behaviour conferring antimicrobial resistance. *Environ Microbiol* 11:126–136. <https://doi.org/10.1111/j.1462-2920.2008.01747.x>.
- Hay NA, Tipper DJ, Gygi D, Hughes C. 1999. A novel membrane protein influencing cell shape and multicellular swarming of *Proteus mirabilis*. *J Bacteriol* 181:2008–2016.
- Tuson HH, Copeland MF, Carey S, Sacotte R, Weibel DB. 2013. Flagellum density regulates *Proteus mirabilis* swarmer cell motility in viscous environments. *J Bacteriol* 195:368–377. <https://doi.org/10.1128/JB.01537-12>.
- Vollmer W, Seligman SJ. 2010. Architecture of peptidoglycan: more data and more models. *Trends Microbiol* 18:59–66. <https://doi.org/10.1016/j.tim.2009.12.004>.
- Wang S, Arellano-Santoyo H, Combs PA, Shaevitz JW. 2010. Actin-like cytoskeleton filaments contribute to cell mechanics in bacteria. *Proc Natl Acad Sci U S A* 107:9182–9185. <https://doi.org/10.1073/pnas.0911517107>.
- Tuson HH, Auer GK, Renner LD, Hasebe M, Tropini C, Salick M, Crone WC, Gopinathan A, Huang KC, Weibel DB. 2012. Measuring the stiffness of bacterial cells from growth rates in hydrogels of tunable elasticity. *Mol Microbiol* 84:874–891. <https://doi.org/10.1111/j.1365-2958.2012.08063.x>.
- Wheeler R, Turner RD, Bailey RG, Salamaga B, Mesnage S, Mohamad SAS, Hayhurst EJ, Horsburgh M, Hobbs JK, Foster SJ. 2015. Bacterial cell enlargement requires control of cell wall stiffness mediated by peptidoglycan hydrolases. *mBio* 6:e00660. <https://doi.org/10.1128/mBio.00660-15>.
- Loskill P, Pereira PM, Jung P, Bischoff M, Herrmann M, Pinho MG, Jacobs K. 2014. Reduction of the peptidoglycan crosslinking causes a decrease in stiffness of the *Staphylococcus aureus* cell envelope. *Biophys J* 107:1082–1089. <https://doi.org/10.1016/j.bpj.2014.07.029>.
- Auer GK, Lee TK, Rajendram M, Cesar S, Miguel A, Huang KC, Weibel DB. 2016. Mechanical genomics identifies diverse modulators of bacterial cell stiffness. *Cell Syst* 2:402–411. <https://doi.org/10.1016/j.cels.2016.05.006>.
- Auer GK, Weibel DB. 2017. Bacterial cell mechanics. *Biochemistry* 56:3710–3724. <https://doi.org/10.1021/acs.biochem.7b00346>.
- Amir A, Babaeipour F, McIntosh DB, Nelson DR, Jun S. 2014. Bending forces plastically deform growing bacterial cell walls. *Proc Natl Acad Sci U S A* 111:5778–5783. <https://doi.org/10.1073/pnas.1317497111>.
- Gan L, Chen S, Jensen GJ. 2008. Molecular organization of Gram-negative peptidoglycan. *Proc Natl Acad Sci U S A* 105:18953–18957. <https://doi.org/10.1073/pnas.0808035105>.
- Patrick JE, Kearns DB. 2012. Swarming motility and the control of master regulators of flagellar biosynthesis. *Mol Microbiol* 83:14–23. <https://doi.org/10.1111/j.1365-2958.2011.07917.x>.
- McLaggan D, Naprstek J, Buurman ET, Epstein W. 1994. Interdependence of K⁺ and glutamate accumulation during osmotic adaptation of *Escherichia coli*. *J Biol Chem* 269:1911–1917.
- Desmarais SM, Tropini C, Miguel A, Cava F, Monds RD, de Pedro MA, Huang KC. 2015. High-throughput, highly sensitive analyses of bacterial morphogenesis using ultra performance liquid chromatography. *J Biol Chem* 290:31090–31100. <https://doi.org/10.1074/jbc.M115.661660>.
- Strating H, Vandenende C, Clarke AJ. 2012. Changes in peptidoglycan structure and metabolism during differentiation of *Proteus mirabilis* into swarmer cells. *Can J Microbiol* 58:1183–1194. <https://doi.org/10.1139/w2012-102>.
- Yao X, Jericho M, Pink D, Beveridge T. 1999. Thickness and elasticity of gram-negative murein sacculi measured by atomic force microscopy. *J Bacteriol* 181:6865–6875.
- Eberhardt C, Kuerschner L, Weiss DS. 2003. Probing the catalytic activity of a cell division-specific transpeptidase in vivo with beta-lactams. *J Bacteriol* 185:3726–3734. <https://doi.org/10.1128/jb.185.13.3726-3734.2003>.
- Chung HS, Yao Z, Goehring NW, Kishony R, Beckwith J, Kahne D. 2009. Rapid beta-lactam-induced lysis requires successful assembly of the cell division machinery. *Proc Natl Acad Sci U S A* 106:21872–21877. <https://doi.org/10.1073/pnas.0911674106>.
- Yao Z, Kahne D, Kishony R. 2012. Distinct single-cell morphological dynamics under beta-lactam antibiotics. *Mol Cell* 48:705–712. <https://doi.org/10.1016/j.molcel.2012.09.016>.
- Tuomanen E, Cozens R, Tosch W, Zak O, Tomasz A. 1986. The rate of killing of *Escherichia coli* by beta-lactam antibiotics is strictly proportional to the rate of bacterial growth. *J Gen Microbiol* 132:1297–1304. <https://doi.org/10.1099/00221287-132-5-1297>.
- Spoering AL, Lewis K. 2001. Biofilms and planktonic cells of *Pseudomonas aeruginosa* have similar resistance to killing by antimicrobials. *J Bacteriol* 183:6746–6751. <https://doi.org/10.1128/JB.183.23.6746-6751.2001>.
- Chen C-Y, Chen Y-H, Lu P-L, Lin W-R, Chen T-C, Lin C-Y. 2012. *Proteus mirabilis* urinary tract infection and bacteremia: risk factors, clinical presentation, and outcomes. *J Microbiol Immunol Infect* 45:228–236. <https://doi.org/10.1016/j.jmii.2011.11.007>.
- Burall LS, Harro JM, Li X, Lockatell CV, Himpl SD, Hebel JR, Johnson DE, Mobley HLT. 2004. *Proteus mirabilis* genes that contribute to pathogenesis of urinary tract infection: identification of 25 signature-tagged mutants attenuated at least 100-fold. *Infect Immun* 72:2922–2938. <https://doi.org/10.1128/iai.72.5.2922-2938.2004>.
- Trivedi RR, Crooks JA, Auer GK, Pendry J, Foik IP, Siryaporn A, Abbott NL, Gitai Z, Weibel DB. 2018. Mechanical genomic studies reveal the role of D-alanine metabolism in *Pseudomonas aeruginosa* cell stiffness. *mBio* 9:e01340-18. <https://doi.org/10.1128/mBio.01340-18>.
- Dobro MJ, Oikonomou CM, Piper A, Cohen J, Guo K, Jensen T, Tadayon

- J, Donermeyer J, Park Y, Solis BA, Kjær A, Jewett AI, McDowall AW, Chen S, Chang Y-W, Shi J, Subramanian P, Iancu CV, Li Z, Briegel A, Tocheva EI, Pilhofer M, Jensen GJ. 2017. Uncharacterized bacterial structures revealed by electron cryotomography. *J Bacteriol* 199:e00100-17.
34. Rojas ER, Billings G, Odermatt PD, Auer GK, Zhu L, Miguel A, Chang F, Weibel DB, Theriot JA, Huang KC. 2018. The outer membrane is an essential load-bearing element in Gram-negative bacteria. *Nature* 559:617–621. <https://doi.org/10.1038/s41586-018-0344-3>.
35. Sliusarenko O, Heinritz J, Emonet T, Jacobs-Wagner C. 2011. High-throughput, subpixel precision analysis of bacterial morphogenesis and intracellular spatio-temporal dynamics. *Mol Microbiol* 80:612–627. <https://doi.org/10.1111/j.1365-2958.2011.07579.x>.
36. CLSI 2000. Methods for dilution antimicrobial susceptibility tests for bacteria that grow aerobically; approved standard. Fifth ed. Clinical and Laboratory Standards Institute, Wayne, PA.
37. Tivol WF, Briegel A, Jensen GJ. 2008. An improved cryogen for plunge freezing. *Microsc Microanal* 14:375–379. <https://doi.org/10.1017/S1431927608080781>.
38. Zheng SQ, Keszthelyi B, Branlund E, Lyle JM, Braunfeld MB, Sedat JW, Agard DA. 2007. UCSF tomography: an integrated software suite for real-time electron microscopic tomographic data collection, alignment, and reconstruction. *J Struct Biol* 157:138–147. <https://doi.org/10.1016/j.jsb.2006.06.005>.
39. Kremer JR, Mastronarde DN, McIntosh JR. 1996. Computer visualization of three-dimensional image data using IMOD. *J Struct Biol* 116:71–76. <https://doi.org/10.1006/jsbi.1996.0013>.
40. Nicastro D, Schwartz C, Pierson J, Gaudette R, Porter ME, McIntosh JR. 2006. The molecular architecture of axonemes revealed by cryoelectron tomography. *Science* 313:944–948. <https://doi.org/10.1126/science.1128618>.
41. Collins TJ. 2007. ImageJ for microscopy. *Biotechniques* 43:25–30. <https://doi.org/10.2144/000112517>.
42. Turner RD, Hurd AF, Cadby A, Hobbs JK, Foster SJ. 2013. Cell wall elongation mode in Gram-negative bacteria is determined by peptidoglycan architecture. *Nat Commun* 4:1496. <https://doi.org/10.1038/ncomms2503>.
43. Kuhner D, Stahl M, Demircioglu DD, Bertsche U. 2014. From cells to muropeptide structures in 24 h: peptidoglycan mapping by UPLC-MS. *Sci Rep* 4:7494. <https://doi.org/10.1038/srep07494>.
44. Glauner B. 1988. Separation and quantification of muropeptides with high-performance liquid chromatography. *Anal Biochem* 172:451–464. [https://doi.org/10.1016/0003-2697\(88\)90468-x](https://doi.org/10.1016/0003-2697(88)90468-x).